PAPER

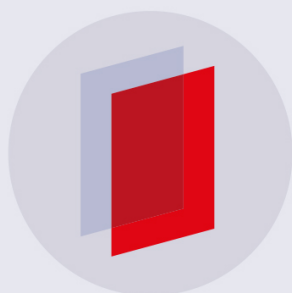# Development of a proximity sensor with vertically monolithic integrated inductive and capacitive sensing units

View the article online for updates and enhancements.

Related content

- A dual-mode proximity sensor with integrated capacitive and temperature sensing units
  Shihua Qiu, Ying Huang, Xiaoyue He et al.

- Development of 3D carbon nanotube interdigitated finger electrodes on polymer substrate for flexible capacitive sensor application
  Chih-Fan Hu, Jhih-Yu Wang, Yu-Chia Liu et al.

- Nanoporous anodic aluminum oxide as a promising material for the electrostatically-controlled thin film interference filter
  Pei-Hsuan Lo, Guo-Lun Luo, Chih-Chun Lee et al.

Recent citations

- A dual-mode proximity sensor with combination of inductive and capacitive sensing units
  Wenqing Kan *et al*

- Development of CMOS MEMS inductive type tactile sensor with the integration of chrome steel ball force interface
  Sheng-Kai Yeh *et al*

- A flexible dual-mode proximity sensor based on cooperative sensing for robot skin applications
  Ying Huang *et al*

IOP ebooks™

Bringing you innovative digital publishing with leading voices to create your essential collection of books in STEM research.

Start exploring the collection - download the first chapter of every title for free.

Development of a proximity sensor with vertically monolithic integrated inductive and capacitive sensing units

Pei-Hsuan Lo[1], Shih-Hsiung Tseng[2], Jen-Hao Yeh[2] and Weileun Fang[1,2]

[1] Institute of NanoEngineering and MicroSystems, National Tsing Hua University, Hsinchu, Taiwan
[2] Power Mechanical Engineering, National Tsing Hua University, Hsinchu, Taiwan

E-mail: fang@pme.nthu.edu.tw

Abstract
This study designs and implements a proximity sensor consisting of inductive and capacitive sensing units. These two sensing units are vertically monolithic integrated on a single chip using the micro-fabrication processes. In addition, low-temperature fabricated nanoporous anodic aluminum oxide (np-AAO) is employed as the dielectric layer to enhance the performance of capacitive sensing. The characteristics of the presented vertically monolithic integrated inductive and capacitive proximity sensor are as follows: (1) enlarged sensing distance of conductive objectives: capacitive sensing unit for short distance detection and inductive sensing unit for long distance detection, (2) non-conductive object can be detected by the capacitive sensing unit, (3) fringe effect capacitive sensing is enhanced by the spiral coil electrode and (4) np-AAO has good dielectric properties (the dielectric constant is 11.9 in this study) for capacitive sensing. In application, various materials (including metal, plastic and a human finger) have been successfully detected by the presented sensor. Preliminary results demonstrate that the typical fabricated proximity sensor has a sensing range of 0.5–5 mm for the metal rod. In comparison, the inductive and capacitive sensing units have the sensing ranges of 1.5–5 and 0.5–3 mm, respectively. Moreover, the non-conductive plastic rod can be detected by the capacitive sensing unit.

(Some figures may appear in colour only in the online journal)

1. Introduction

The proximity sensor is one of the important devices for the applications of robot [1], industrial monitoring, mobile phone, automobile, etc. The proximity sensor has been widely used for position detection to prevent physical contact between objects. Many sensing techniques have been developed for proximity sensors so far. For instance, capacitive-, inductive-, infrared- and ultrasonic-type proximity sensors have been respectively reported in [2–5]. To further extend the applications of proximity sensors, size reduction and reduced cost become two critical concerns for the device design and implementation. In this regard, the micro-electromechanical systems (MEMS) technology is a promising approach to implement proximity sensors. Compact size proximity sensors could be batch fabricated using micromachining technology.

The inductive- and capacitive-type proximity sensors have a relatively simple structure, and can be easily fabricated. The inductive-type proximity sensor has the characteristic of water and oil resistance, and thus can be operated in a contaminated environment [6]. Several approaches have been reported to achieve the inductive proximity sensor, such as composite materials spiral wire [7] and multi-structure spiral wire [8]. The inductive proximity sensor is suitable for detecting conductive targets, but is less sensitive to objects with low conductivity and non-magnetic materials (such as the human body) [9]. In addition, the inductive sensing technique is less sensitive to detect an object within a short distance of the sensor [10]. The variation of the fringe electric field as well as the parallel plate electric field has been exploited to develop the capacitive-type proximity sensor. For the parallel-plate-type proximity sensor, a stationary plate and the object to
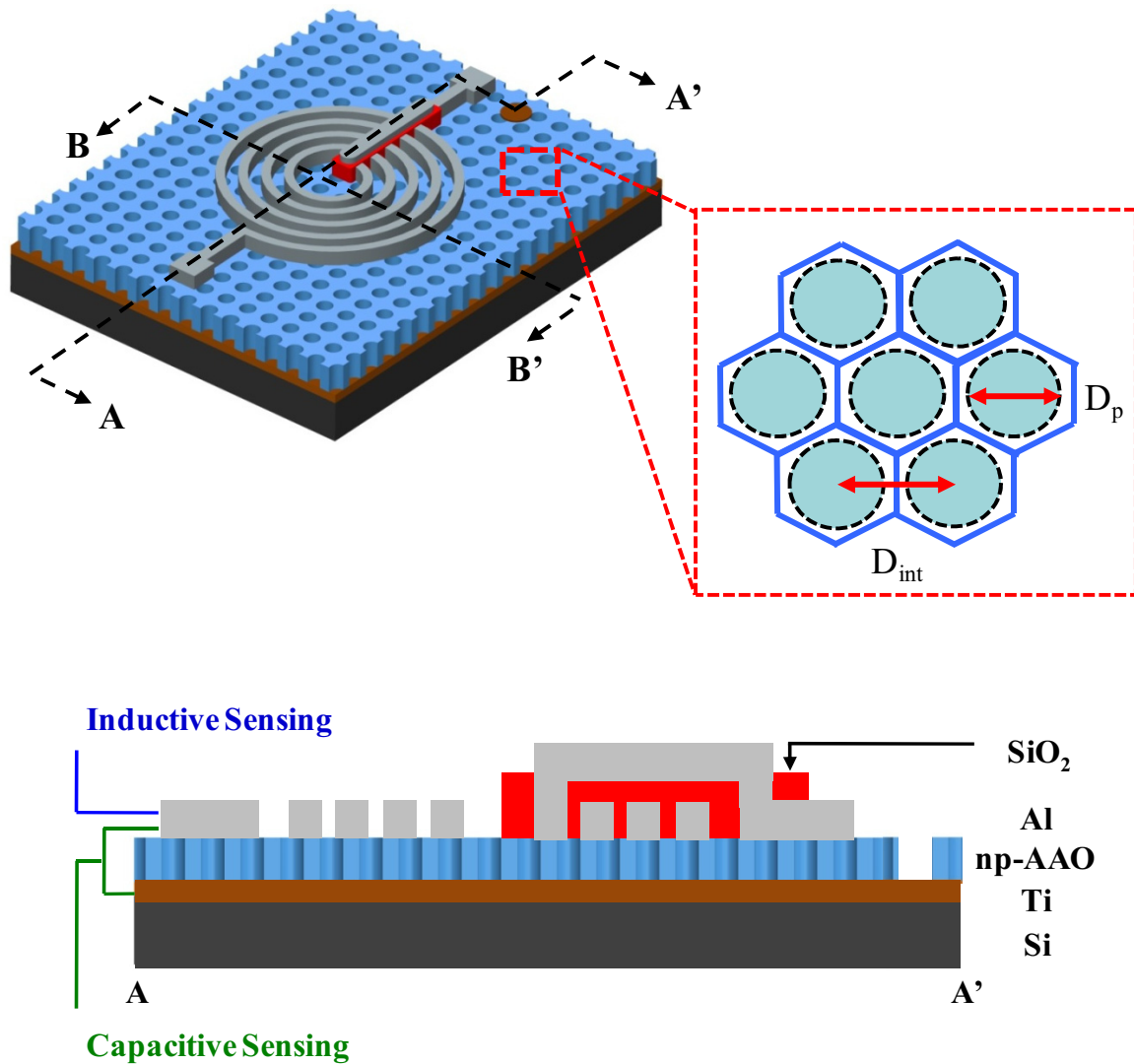
Figure 1. The device architecture of the present vertically monolithic integrated inductive and capacitive proximity sensor. The cross section AA′ shows the proximity sensor consisted of metal films (Ti electrode and Al spiral coil), SiO$_2$ and np-AAO dielectric layer.

be detected form the parallel plate electric field [11]. The capacitance between such parallel plates will be changed as the distance between the moving object and the stationary plate is varied. Despite its wide applications, the parallel-plate-type proximity sensor can only detect conductive objects. For fringe effect-type proximity sensor, the sensing objects could be either conductors or non-conductors. Moreover, the fringe effect proximity sensor has excellent short distance sensing capability [11–12]. However, the sensing distance of the fringe effect proximity sensor is limited by the distribution of the fringe electric field. It is possible to enhance the variety of sensing objects and also increase the sensing range of the proximity sensor by integrating the inductive and capacitive sensing units. A novel proximity sensor to integrate bulk coil inductive and capacitive sensing units side by side has been reported in [13]. The concept gives inspiration to the possibility of integrating inductive and capacitive proximity sensors using MEMS technology.
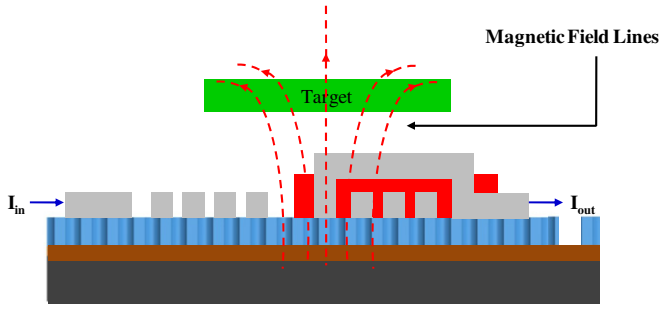
This study presents the concept of vertical monolithic integrating the inductive and capacitive proximity sensing

devices on a single chip. Thus, the range of the sensing distance can be enlarged. In addition, both conductive and non-conductive objects can be detected. The vertical monolithic integration of the sensing units using micro-fabrication technology can significantly reduce the size of the proximity sensor. This study establishes the processes to implement the presented proximity sensor. To further improve the performance of the proximity sensor, nanoporous anodic aluminum oxide (np-AAO) material with a high dielectric constant is employed as the dielectric layer in this sensing device. In this study, we have characterized the sensing distance of the sensor, and also investigated the variation of output inductance and capacitance with sensing objects of various materials.

2. Concept and design

The schematic illustration in figure 1 shows the device architecture of the present vertically monolithic integrated inductive and capacitive proximity sensors with an np-AAO

(*a*) **Inductive Sensing (AA')**

Magnetic Field Lines

Target

I_{in} I_{out}

(*b*) **Capacitive Sensing (BB')**

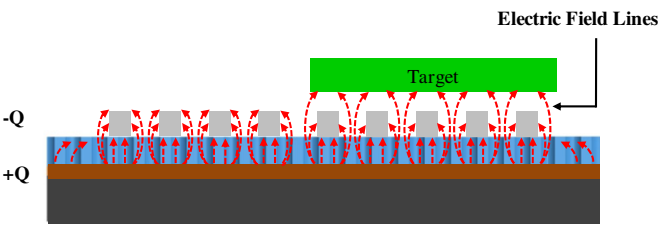**Electric Field Lines**

Target

-Q

+Q

Figure 2. The sensing mechanism of the proposed proximity sensor with two different sensing units: (*a*) the cross section of AA′ indicates the inductive sensing by the magnetic field introduced from the Al spiral coil, and (*b*) the cross section BB′ depicts the capacitive sensing by the fringe electric field generated from the Al spiral coil upper electrode and the Ti lower electrode.

Figure 3. Some important dimensions of the presented circular spiral coil.

nanostructure. In this design, the proximity sensor consists of various vertically stacked layers. The Ti and np-AAO are fabricated on top of the Si substrate to respectively serve as the lower electrode and the dielectric layer. Another Al spiral is further deposited on the np-AAO layer as the upper electrode. The upper and lower electrodes form the capacitive sensing unit. Moreover, the Al spiral also acts as the coil for the inductive sensing unit. This study exploits np-AAO as a superior dielectric material [14–15]. In general, the np-AAO film usually has been exploited to act as a template or mask for nano-technology applications, such as nanowires synthesis and nano-structures [16–17]. The superior electrical characteristics of the np-AAO film have also been investigated in [18–21]. As reported in [22], the dielectric properties of np-AAO could be influenced by the porous structure, such as the interpore distance (D_{int}), nanopore diameter (D_p) and pore depth. In this study, np-AAO of higher dielectric constant is employed to improve the initial capacitance as well as the performance of the capacitive proximity sensor. Other high dielectric materials, such as HfO_2, Ta_2O_5 and ZrO_2, have also been reported. However, high temperature (500–700 °C) and complicated fabrication processes are required. To enable the future integration of high dielectric material above IC, the process temperature would be a critical concern. The low-temperature (7 °C) prepared np-AAO film could meet the thermal budget of the IC process. Moreover, such np-AAO process platform has the potential to enable the fabrication and monolithic integration of various sensors [23–24].

Figures 2(*a*) and (*b*) respectively show two different sensing approaches of the presented vertically monolithic
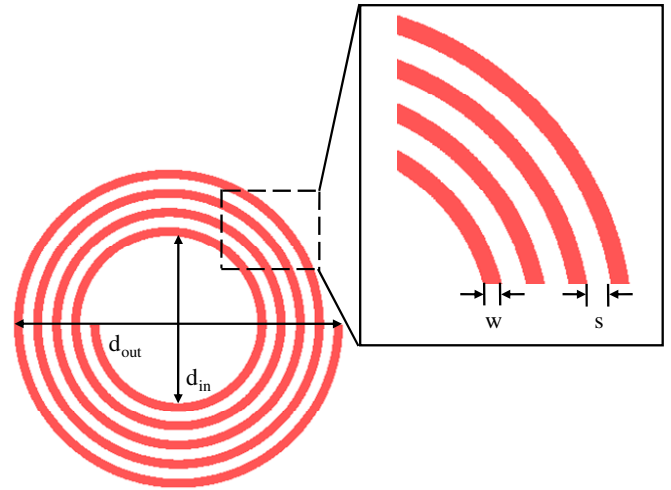
integrated proximity sensor. The Al spiral in figure 2(*a*) acts as an inductive coil. The magnetic field from the metal spiral enables inductive sensing after applying an ac-signal. As an object approaches the spiral, the magnetic flux will be changed. Hence, the object is detected by the inductance change of the spiral. By using the model established in [25–26], the electrical inductance L of the circular spiral coil employed in this study (as shown in figure 3) is expressed as

$$ L \cong \frac{\mu_0 n^2 d_{avg} c_1}{2} \left[\ln\left(\frac{c_2}{F}\right) + c_3 F + c_4 F^2 \right], \qquad (1) $$

where n is the number of turns of the spiral coil, d_{avg} is the average diameter of the coil windings and $F = (d_{out} - d_{in})/(d_{out} + d_{in})$ is the fill factor of the coil windings. The permeability constant μ_0 is $4\pi \times 10^{-7}$ (in henries per meter). Moreover, the geometric coefficients for the circular spiral are $c_1 = 1$, $c_2 = 2.46$, $c_3 = 0$ and $c_4 = 0.2$, respectively [27].

Moreover, the Al spiral and the Ti film in figure 2(*b*) form the electrodes for capacitive sensing. The electric field (including the fringe electric field) is schematically illustrated in the figure. Thus, the fringe capacitance between the metal spiral upper electrode and the Ti lower electrode enable the capacitive sensing. Since the inductive and fringe field capacitive sensing devices are respectively employed for long distance and short distance proximity detecting, the range of the sensing distance is enlarged by the present design. The fringing capacitance is significantly influenced by the geometrical pattern of the sensing electrode [28]. Thus, as compared with the conventional rectangular parallel plate electrode [29], the spiral coil electrode could increase the fringe sensing capacitance. The commercial finite element software (ANSOFT Maxwell) is employed to simulate the distribution of the electric field for parallel plate sensing electrodes. Both the magnitude and direction of the electric field are indicated by the arrows and colors. The fringe electric fields for both square and spiral electrodes are respectively displayed in figures 4(*a*) and (*b*). As indicated in figure 4(*a*), the approaching object mainly influences the distribution of the fringe electric field, and further causes the capacitance change of the proximity sensor. This simulation result agrees with
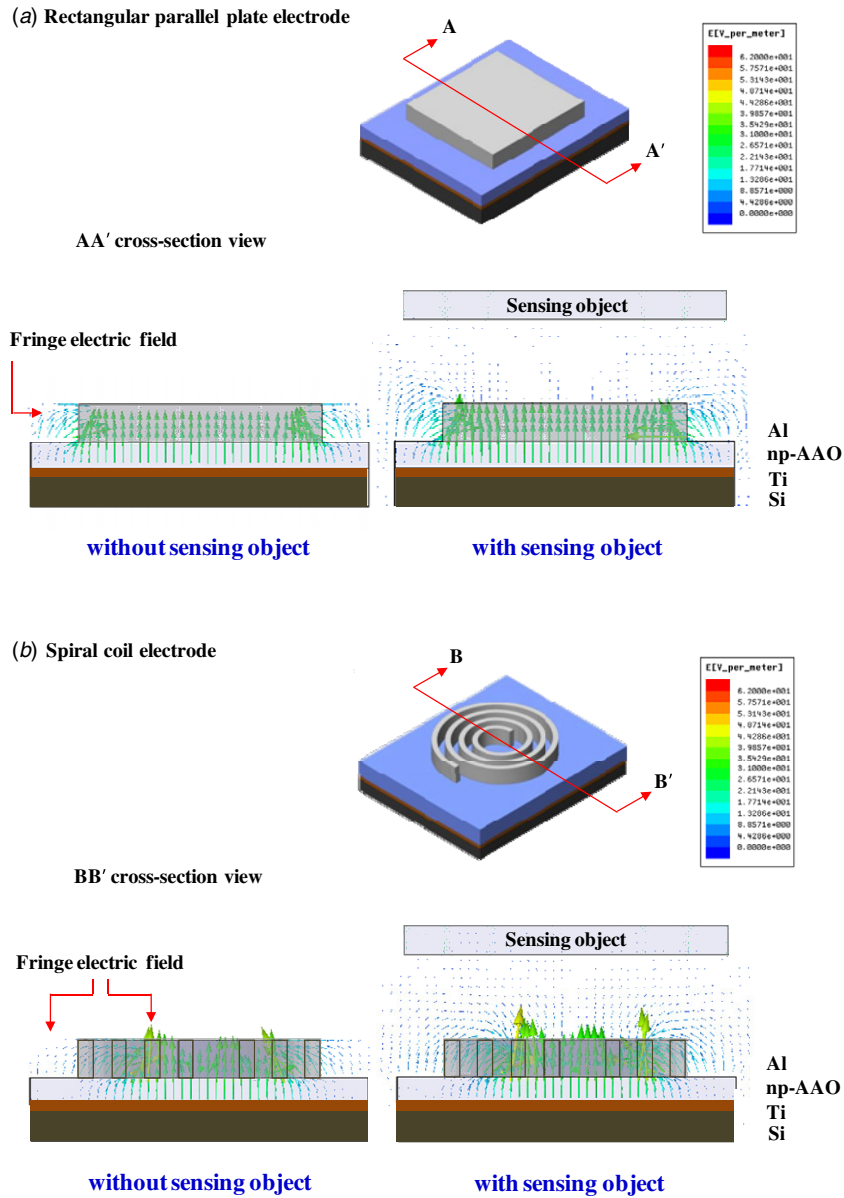
(*a*) **Rectangular parallel plate electrode**

AA′ cross-section view

without sensing object   **with sensing object**

(*b*) **Spiral coil electrode**

BB′ cross-section view

without sensing object   **with sensing object**

Figure 4. The simulation results of fringe electric field lines distribution between: (*a*) the rectangular parallel plate electrodes, and (*b*) the presented circular spiral coil upper electrode and the rectangular plate lower electrode.

the discussion in [1, 11–13]. In this regard, in this study, we design the spiral coil to increase the perimeter of electrodes. As depicted in figure 4(*b*), the distribution of the fringe electric field has been increased. Thus, as an object approaches, the distribution of the fringe electric field along the perimeter of the spiral coil is influenced. As a result, the variation of electric field is increased so as to enhance the magnitude of the sensing capacitance.

Moreover, the measured capacitance of the sensor can be expressed as

$$C = \frac{\varepsilon \cdot \varepsilon_0 \cdot A}{t}, \qquad (2)$$

where ε and t are respectively the dielectric constant and thickness of the np-AAO dielectric layer, A is the area of the metal electrode and ε_0 is permittivity in the air ($\varepsilon_0 \approx 8.854 \times 10^{-12}$ in farads per meter). According to the

higher dielectric constant of the np-AAO film, the capacitive proximity sensor has superior performance.

3. Fabrication and results

The fabrication processes to implement the presented sensor are displayed in figure 5. As shown in figure 5(*a*), the 100 nm thick Ti film and 330 nm thick Al film were deposited onto the Si substrate. The Ti and Al films were respectively acting as the lower electrode and the layer for the following np-AAO. After that, the Al film was etched by using the two-step anodization technique [30–31] to implement the np-AAO layer, as illustrated in figures 5(*b*)–(*d*). The dielectric constant can be improved as the np-AAO has uniform interpore distance and nanopore diameter. In other words, the dielectric constant of np-AAO could be modified by the anodization process conditions for the np-AAO film, such as anodization
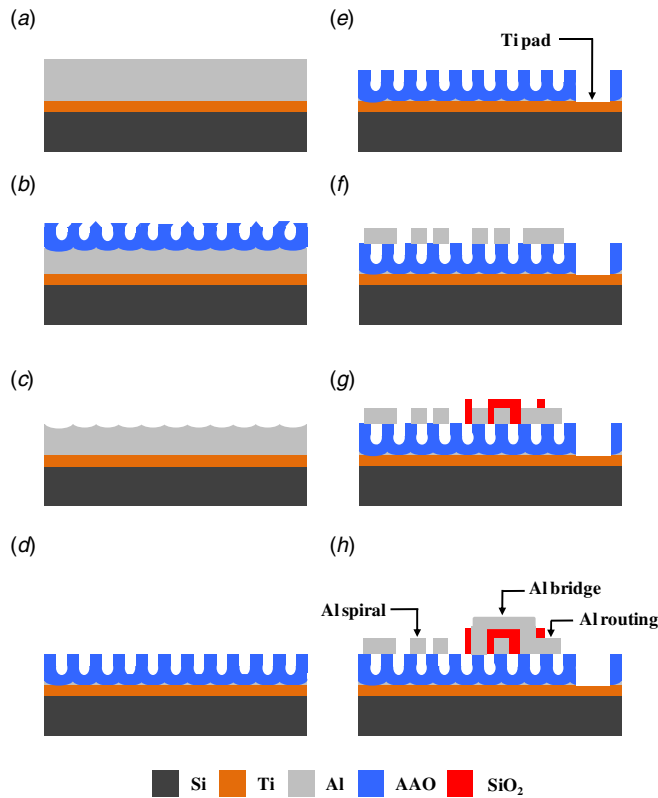
Figure 5. Fabrication process steps: (*a*) deposited Ti/Al on Si substrate, (*b*)–(*d*) anodization of Al to form the np-AAO, (*e*) Ti electrode contact pad was defined, (*f*) Al film was evaporated on np-AAO and patterned as spiral coil, (*g*) SiO$_2$ was deposited as the insulation layer and (*h*) Al was evaporated and patterned as the bridge for electrical routing.

Figure 6. Fabrication results: (*a*) optical micrograph of the typical fabricated sensor; and FE-SEM micrographs of (*b*) metal and insulation films stacking on the Si substrate, (*c*), (*d*) Al bridge, Al spiral coil and Al electrical routing, and (*e*), (*f*) top view and side view of the np-AAO structures.

temperature, voltage and time [21]. The two-step anodization process could improve the uniformity of interpore distance and nanopore diameter for the np-AAO film and further increase its dielectric constant. Moreover, various pre-treatment methods such as the SiC mold imprint lithography or direct focused-ion-beam lithography have been reported in [31] to further enhance the regular arrangement of pores. These pre-treatment techniques could further improve the dielectric constant of the np-AAO film. During the first anodization process, the substrate was first immersed into a 7 °C aqueous solution with 0.3M oxalic acid (H$_2$C$_2$O$_4$) at the voltage of 40 V dc [16], and the np-AAO layer was formed on top of the Al film, as shown in figure 5(*b*). The substrate was then immersed into the mixture of chromic acid (1.8 wt%) and phosphoric acid (6 wt%) at 70 °C to remove the np-AAO formed on top of the Al film, as depicted in figure 5(*c*). After that, the substrate underwent the second anodization process with the same process conditions as the first one. As shown in figure 5(*d*), the substrate was covered with a 100 nm thick Ti film and a 300 nm thick np-AAO layer after the above two-step anodization processes. The np-AAO with self-organized nanopores was exploited as the dielectric layer for the presented vertically monolithic integrated inductive and capacitive sensor. The size of the nanopores would influence the dielectric constant of np-AAO [22]. Thus, the processing parameters, such as temperature, input voltage and current, anodizing time and electrolyte were
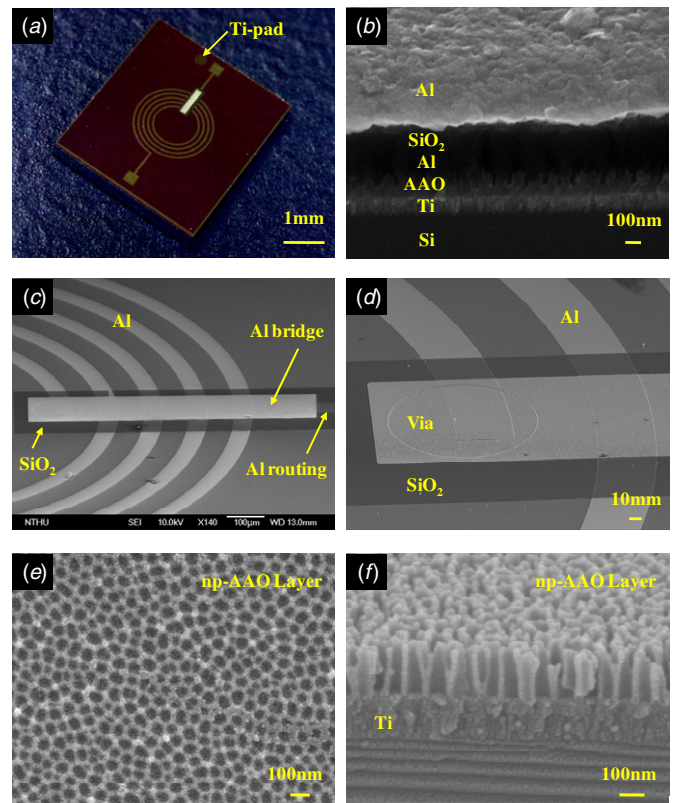
employed to control the diameter and length of the nanopores. As illustrated in figure 5(*e*), the np-AAO was etched by a mixture of chromic acid (1.8 wt%) and phosphoric acid (6 wt%) at 70 °C, and defined the bond pad for the lower electrode. As shown in figure 5(*f*), the Al film was evaporated on top of the np-AAO and then patterned as a spiral coil. The SiO$_2$ film (500 nm) in figure 5(*g*) was then deposited and patterned as the insulation layer. After that, the second Al film was deposited and patterned as the electrical interconnection between Al spiral and Al routing, as indicated in figure 5(*h*).

The photo in figure 6(*a*) shows the top view of the typical fabricated proximity sensor on chip. The spiral coil on the chip of 5 mm × 4 mm is clearly observed. The field emission scanning electron microscope (FE-SEM, JOEL JSM-7000F) image in figure 6(*b*) shows the stacking of different layers on the Si substrate for a typical fabricated sensor. The FE-SEM micrograph in figure 6(*c*) shows the Al bridge and Al spiral. In this study, the proximity sensor has an Al spiral of 4.5 turns with the inner diameter of $d_{in} = 1000$ μm, outer diameter $d_{out} = 2060$ μm, line width $w = 50$ μm and line spacing $s = 70$ μm. The micrograph in figure 6(*d*) further shows a zoom of the Al bridge and Al spiral. The FE-SEM micrograph in figure 6(*e*) shows the top view of the AAO film with nanopores, and the nanopore diameter ranges 50–60 nm. Finally, the micrograph in figure 6(*f*) depicts the cross-section of np-AAO with columnar structures.
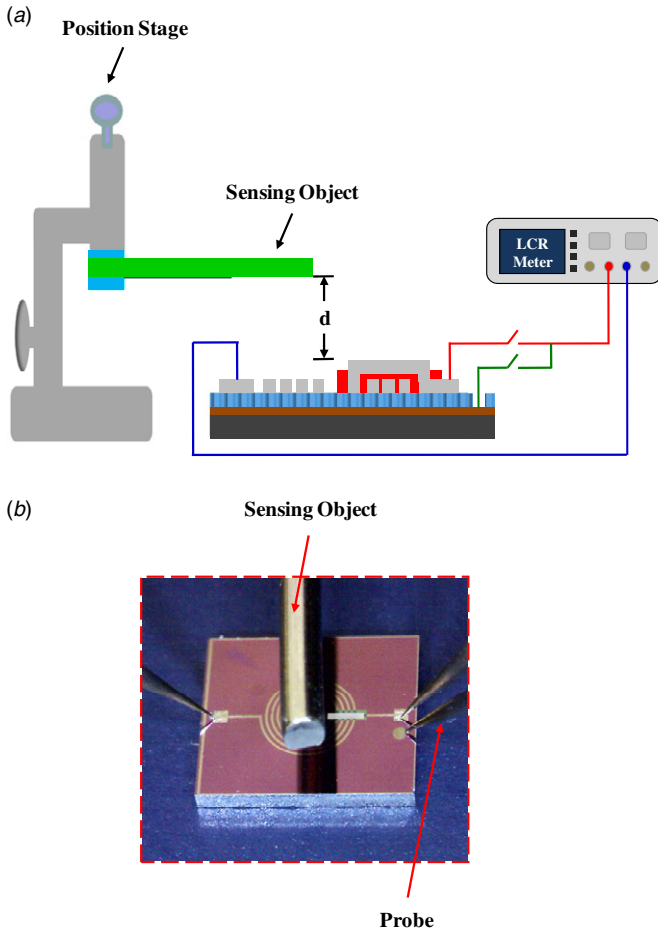
(*a*)

(*b*)

Figure 7. (*a*) Measurement setup for proximity sensing test, and (*b*) metal rod as a typical sensing object on top of the proximity sensor.

4. Experiments and discussions

Figure 7 shows the experiment setup to characterize the performances of the sensor. Figure 7(*a*) shows the electrical routings for the inductive and capacitive proximity sensing. The LCR meter (Agilent E4980A) is used to apply an ac signal of 2 MHz to the spiral coil. Thus, the spiral coil could generate a magnetic field for inductive sensing. On the other hand, the spiral coil and the Ti film could generate an electric field for capacitive sensing. Meanwhile, the inductance and capacitance of sensing units are also measured by using the LCR meter through the three-probe method, and then recorded by computer. Moreover, the fixture and stage are employed to tune the object position for the proximity sensing test. The distance *d* between the sensing object and the proximity sensor can be precisely controlled. The photo in figure 7(*b*) shows the metal rod as a typical sensing object on top of the proximity sensor chip for the test. The diameter and length of metal rod are 0.7 and 7 mm, respectively.

The measurement results in figure 8 respectively show the variation of inductance and capacitance with the distance *d* between the sensing object (metal rod in figure 7(*b*)) and the proximity sensor. Measurements in figure 8(*a*) indicate the sensing inductance increases from 40.62 to 41.84 nH as the metal rod moves from $d = 6$ mm to $d = 1.5$ mm. Thus, the
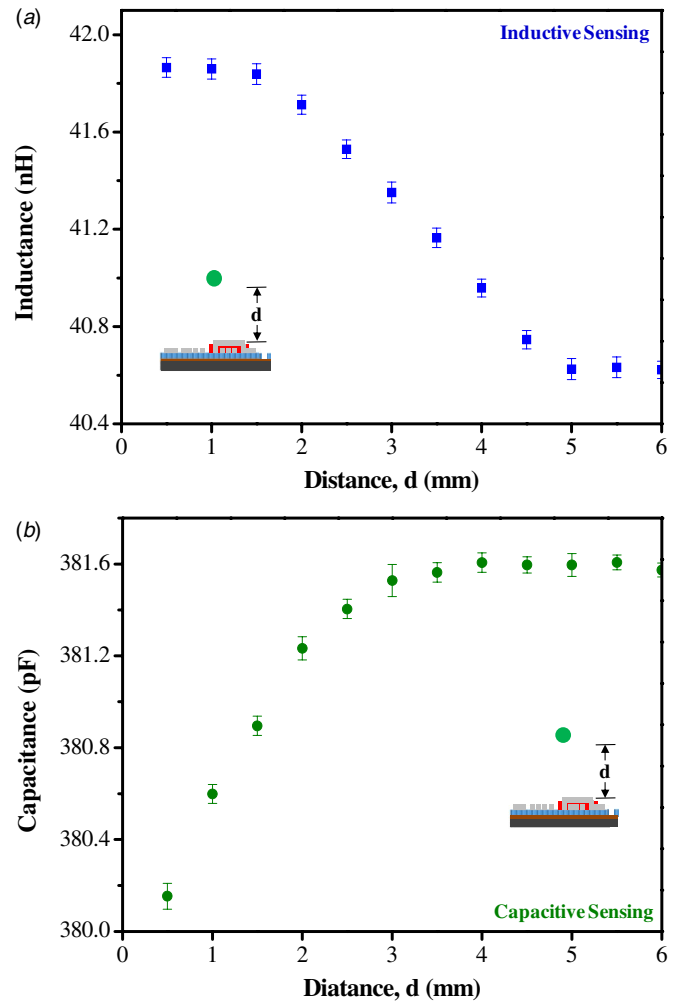
(*a*)

(*b*)

Figure 8. The metal rod proximity sensing tests at different distances *d* from the sensor: (*a*) inductance change detected by the inductive sensing unit, and (*b*) capacitance change detected by the capacitive sensing unit.

inductive proximity sensor has a sensitivity of 0.35 nH mm^{-1} (and nonlinearity of 3.27%) to the metal rod within the sensing distance of $d = 1.5$–5.0 mm. The results also indicate that the inductance of spiral coil proximity sensor will not be influenced by the metal rod if the distance is $d > 5$ mm or $d < 1.5$ mm. Measurements in figure 8(*b*) depict the sensing capacitance decreases from 381.53 to 380.15 pF as the metal rod moves from $d = 3$ mm to $d = 0.5$ mm. Hence, the capacitive proximity sensor has a sensitivity of 0.55 pF mm^{-1} (and nonlinearity of 9.84%) to the metal rod within the sensing distance of $d = 0.5$ mm–3.0 mm. The capacitance of sensing electrodes will not be influenced by the metal rod as their distance is $d > 3$ mm. Moreover, the measured initial capacitance of the proximity sensor (with no sensing object) is 381.57 pF. According to equation (2), the dielectric constant of the np-AAO film is determined to be $\varepsilon_{np\text{-}AAO} = 11.9$ (at 2 MHz), which is threefold higher than that of SiO$_2$ ($\varepsilon_{SiO2} = 3.9$). Note the inductive sensing is insensitive to the object at a sensing distance less than 1.5 mm and greater than 5.0 mm. The capacitive sensing is insensitive to the object at sensing distance greater than 3.0 mm. Thus, the proposed proximity
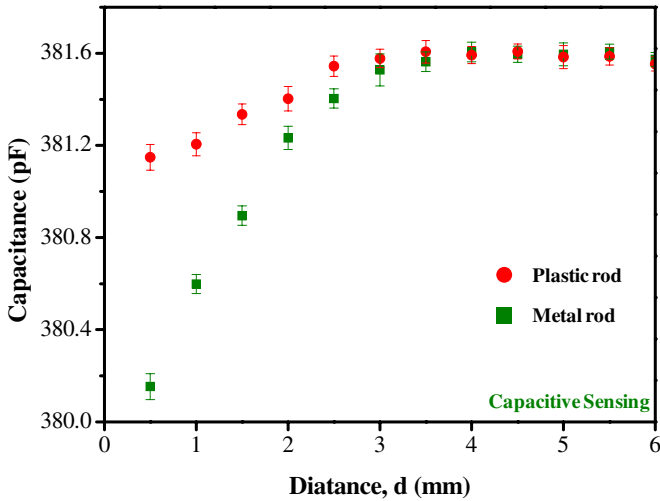
Figure 9. Comparison of measured capacitance change between metal and plastic rods.

sensor with both inductive and capacitive sensing units can extend the range of the sensing distance to $d = 0.5$–5.0 mm.

In comparison, this study has also employed objects of different materials, such as the finger and plastic rod (insulating material), for proximity sensing tests. Measurements in figure 9 show the variation of capacitance with the distance d between the plastic rod and the proximity sensor. The size of the plastic rod (with diameter of 0.74 mm and length of 7 mm) is about the same as that of the metal rod. The sensing capacitance decreases from 381.58 to 381.15 pF as the plastic rod moves from $d = 3$ mm to $d = 0.5$ mm. Thus, the capacitive proximity sensor has a sensitivity of 0.172 pF mm^{-1} (and nonlinearity of 7.04%) to the plastic rod within the sensing distance of $d = 0.5$–3.0 mm. The measurements for the metal rod are also displayed for comparison. The capacitance sensing has mainly resulted from the fringe effect of sensing electrodes. This study could not predict the fringe sensing capacitance change by analysis so far. The variation of the sensing capacitance with the proximity distance for various materials has also been reported in [1]. As compared with the insulator, the conductive object has a higher sensing capacitance at a given distance with the capacitive proximity sensor. Moreover, the plastic rod could not be detected by the inductive sensing unit. Figure 10 further shows the sensing signals detected by the proximity sensor during the intermittent (every 5 s) approach of the metal and plastic rods. Measurements in figure 10(a) indicate the inductance change for the metal rod is 0.50 nH at the sensing distance of $d = 3.5$ mm. However, the inductance change for the plastic rod (also at the sensing distance of $d = 3.5$ mm) could not be detected by the presented proximity sensor. Moreover, measurements in figure 10(b) show the capacitance changes for the metal rod and the plastic rod are respectively 0.67 and 0.2 pF at the same sensing distance of $d = 1.5$ mm. In summary, as compared with the capacitive sensing unit, the inductive sensing unit is insensitive to the insulating materials (plastic rod).

Figure 11 further shows the sensing signals recorded by the proximity sensor during the intermittent (every 5 s) approach of two different objects (metal rod and finger).
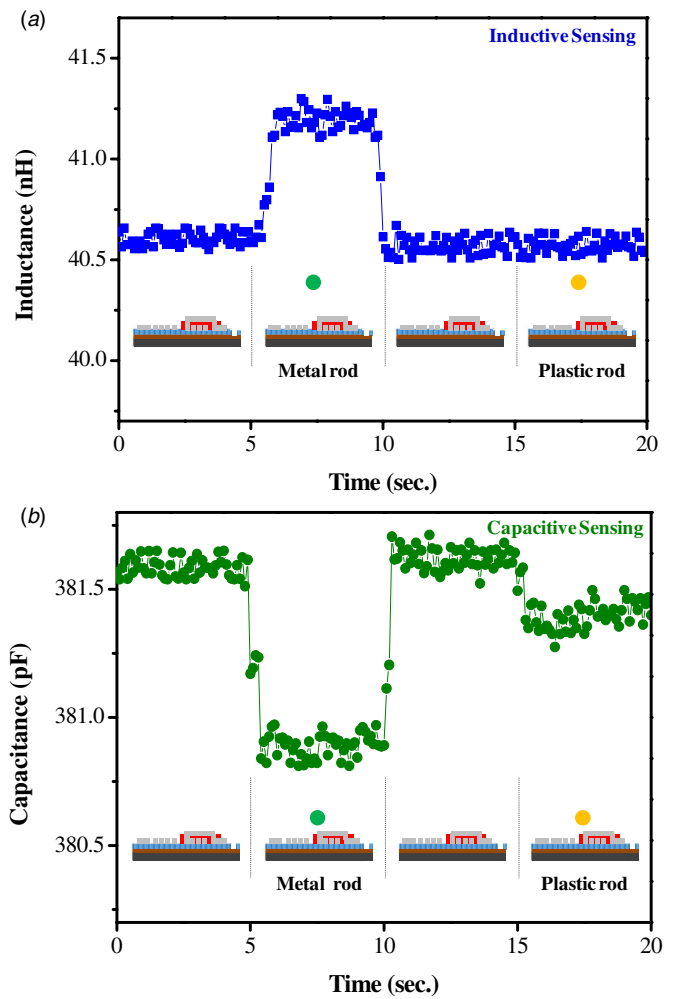

Figure 10. Measurement results show sensing signals detected by (a) inductive sensing unit and (b) capacitive sensing unit, during the intermittent approach of the metal rod and plastic rod.

Measurements in figure 11(a) indicate the inductance changes for the metal rod and finger are respectively 0.86 and 0.09 nH at the same sensing distance of $d = 3.5$ mm. In addition, measurements in figure 11(b) show the capacitance changes for the metal rod and finger are respectively 0.87 and 0.62 pF at the same sensing distance of $d = 1.5$ mm. As compared with the capacitive sensing unit, the sensitivity difference between the metal rod and finger for the inductive sensing unit is much larger. The capacitive proximity sensor of 4.5 turns spiral coil upper electrode has been implemented and tested for the previous discussions in this study. To compare the fringe electric field, different configurations of upper electrodes (including the 4.5 turns spiral, and rectangular plate) have also been designed, implemented and tested. To make a fair comparison, these two electrodes are designed to have the same surface area (surface area is 1081 492 μm^2). The metal rod with 0.7 mm diameter and 7 mm length (same as the metal rod used in the experiments in figures 8 and 10) is employed as the object to characterize the capacitance sensing of the proximity sensor. Measurements in figure 12 depict the variation of capacitance change ($\Delta C/C_0$) with distance d for sensors of different upper electrodes. It demonstrates that
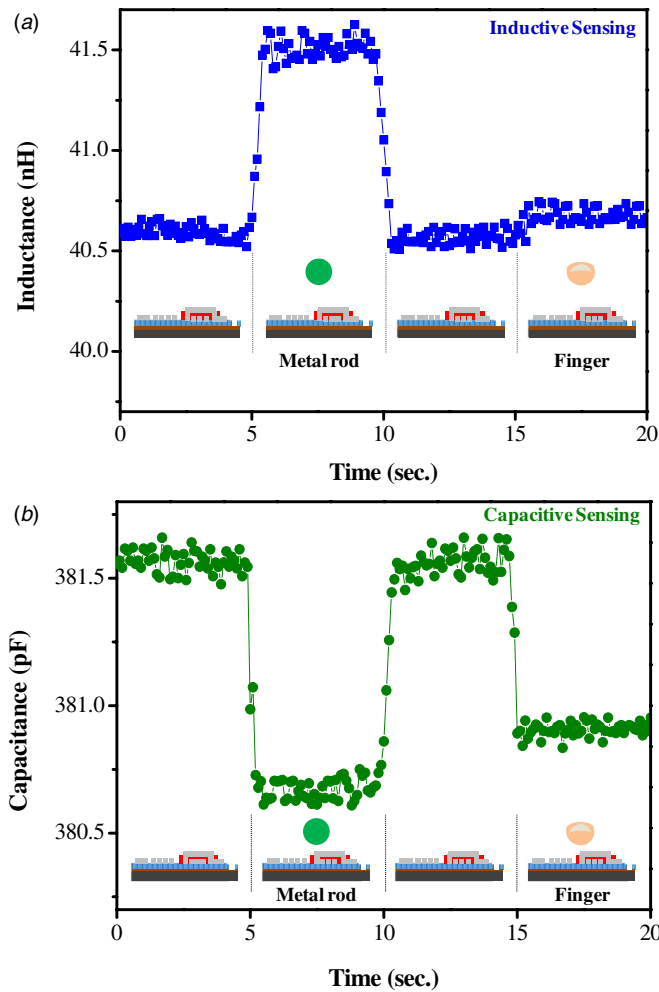
Figure 11. Measurement results show sensing signals detected by (*a*) inductive sensing unit and (*b*) capacitive sensing unit, during the intermittent approach of the metal rod and finger.
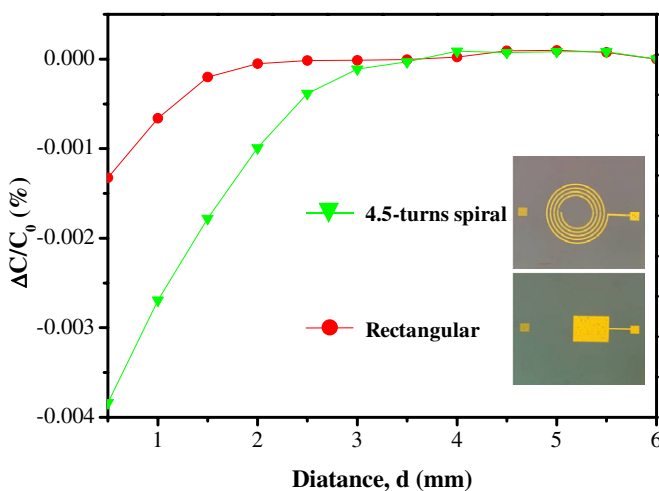

Figure 12. Comparison of measured capacitance changes using the capacitive sensing devices of different upper electrode designs (rectangular plate and circular spiral coil upper electrodes).

higher sensing capacitance as well as longer sensing range could be achieved by the spiral coil electrode design. Thus, the spiral electrode, which also acted as the inductive coil for

the presented integrated sensor, could offer the advantage of increasing the fringe electric field.

5. Conclusions

In summary, the major contribution of this study is to vertically integrate inductive and capacitive proximity sensors on a single chip. As compared with the side-by-side integrated sensors, the sensing pixel is reduced by the vertically integrated design. As opposed to the side-by-side integrated sensors, the vertically stacked inductive and capacitive sensing pixels have no offset in the in-plane position. In addition, this study successfully established the micro-fabrication processes to implement the presented sensor on chip. Moreover, proximity sensing tests using the fabricated proximity sensor have been performed on objects of different materials such as metal, plastic and a human finger. Measurements demonstrate that the sensing range of a typical fabricated proximity sensor is 0.5–5 mm for the metal rod. In comparison, the inductive and capacitive sensing units have the sensing ranges of 1.5–5 and 0.5–3 mm, respectively. The non-conductive plastic rod can also be detected by the capacitive sensing unit. However, the sensing range for the non-conductive object could not be enlarged by using the inductive sensing unit. The np-AAO with high dielectric constant has been prepared using low temperature and uncomplicated fabrication process to increase the performance of the capacitive sensing unit. It would be useful to investigate the variation of the np-AAO dielectric constant with the dimensions of interpore distance, nanopore diameter and pore depth. The dominant factors for the performance of np-AAO-based capacitive proximity sensors will be further analyzed in future experiments.

Acknowledgments

References

[1]　Lee H-K, Chang S-I and Yoon E 2009 Dual-mode capacitive proximity sensor for robot application: implementation of tactile and proximity sensing capability on a single polymer platform using shared electrodes *IEEE Sensors J.* **9** 1748–55

[2]　Bell D J, Lu T J, Fleck N A and Spearing M 2005 MEMS actuators and sensors: observations on their performance and selection for purpose *J. Micromech. Microeng.* **15** S153–64

[3]　Rogner A, Eicher J, Munchmeyer D, Peters R-P and Mohr J 1992 The LIGA technique—what are the new opportunities *J. Micromech. Microeng.* **2** 133–40

[4]　Um D, Ryu D and Kal M 2011 Multiple intensity differentiation for 3-D surface reconstruction with mono-vision infrared proximity array sensor *IEEE Sensors J.* **11** 3352–8

[5] Min S-D, Kim J-K, Shin H-S, Yun Y-H, Lee C-K and Lee M 2010 Noncontact respiration rate measurement system using an ultrasonic proximity sensor *IEEE Sensors J.* **10** 1732–9

[6] Jagiella M, Fericean S and Dorneich A 2006 Progress and recent realizations of miniaturized inductive proximity sensors for automation *IEEE Sensosr J.* **6** 1734–41

[7] Sadler D J and Ahn C H 2001 On-chip eddy current sensor for proximity sensing and crack detection *Sensors Actuators* A **91** 340–5

[8] Velten T, Stefan D and Obermeier E 1999 Micro-coil with movable core for application in an inductive displacement sensor *J. Micromech. Microeng.* **9** 119–22

[9] Zitouni A, Beheim L, Huez R and Belloir F 2006 Smart electromagnetic sensor for buried conductive targets identification *IEEE Sensors J.* **6** 1580–91

[10] Reininger T, Welker F and von Zeppelin M 2006 Sensors in position control applications for industrial automation *Sensors Actuators* A **129** 270–4

[11] Luo R C 1996 Sensor technologies and microsensor issues for mechatronics systems *IEEE ASME Trans. Mechatronics* **1** 39–49

[12] Wang D-C, Chou J-C, Wang S-M, Lu P-L and Liao L-P 2003 Application of a fringe capacitive sensor to small-distance measurement *Japan. J. Appl. Phys.* **42** 5816–20

[13] George B, Zangl H, Bretterklieber T and Brasseur G 2010 A combined inductive-capacitive proximity sensor for seat occupancy detection *IEEE Trans. Instrum. Meas.* **59** 1463–70

[14] Kisner A, Aguiar M R, Vaz A F, Rojas A, Cavarsan F A, Diniz J A and Kubota L T 2009 Submicrometer-MOS capacitor with ultra high capacitance biased by Au nanoelectrodes *Appl. Phys.* A **94** 831–6

[15] Liang C, Terabe K, Hasegawa T and Aono M 2007 Resistance switching of an individual Ag_2/Ag nanowire heterostructure *Nanotechnology* **18** 485202

[16] Kim D, Hwang W, Park H C and Lee K-H 2006 Superhydrophobic nano-wire entanglement structures *J. Micromech. Microeng.* **16** 2593–7

[17] Kim D-H, Kim Y, Kim B M, Ko J S, Cho C-R and Kim J-M 2011 Uniform superhydrophobic surfaces using micro/nano complex structures formed spontaneously by a simple and cost-effective nonlithographic process based on anodic aluminum oxide technology *J. Micromech. Microeng.* **21** 45003–10

[18] Lo P-H, Hong C, Tseng S-H, Yeh J-H and Fang W 2012 Implementation of vertical-integrated dual mode inductive-capacitive proximity sensor *MEMS: IEEE 25th Int. Conf. Micro Electro Mechanical Systems (Paris, France)* pp 640–3

[19] Lazzara T D, Lau K H A, Knoll W, Majoral J-P, Caminade A-M, Janshoff A and Steinem C 2012 Macromolecular shape and interactions in layer-by-layer assemblies within cylindrical nanopores *Beilstein J. Nanotechnol.* **3** 475–84

[20] Hong C, Chu L, Chiang A-S and Fang W 2011 Implementation of a new capacitive touch sensor using the nanoporous anodic aluminum oxide (np-AAO) structure *IEEE Sensors J.* **11** 1748–55

[21] Jung Y W, Byun J S, Woo D H and Kim Y D 2009 Ellipsometric analysis of porous anodized aluminum oxide films *Thin Solid Films* **517** 3726–30

[22] Sohn J I, Kim Y-S, Nam C, Cho B K and Seonga T-Y 2005 Fabrication of high-density arrays of individually isolated nanocapacitors using anodic aluminum oxide templates and carbon nanotubes *Appl. Phys. Lett.* **87** 123115

[23] Chang H-C, Hung S-S, Lai C-C, Chen Y-H, Chang I-N, Lin J-C and Liu T-C 2012 Nano-AAO-based microsensor for monitoring process carbon monoxide *Adv. Mater. Res.* **468–471** 2136–40

[24] Graham A H D, Bowen C R, Robbins J and Taylor J 2009 Formation of a porous alumina electrode as a low-cost CMOS neuronal interface *Sensors Actuators* B **138** 296–303

[25] Terman F E 1943 *Radio Engineers' Handbook* (New York: McGraw-Hill)

[26] Lee T H 2004 *The Design of CMOS Radio-Frequency Integrated Circuits* 2nd edn (New York: Cambridge University Press)

[27] Mohan S S, del Mar Hershenson M, Boyd S P and Lee T H 1999 Simple accurate expressions for planar spiral inductances *IEEE J. Solid-State Circuits* **34** 1419–24

[28] Chen Z and Luo R C 1998 Design and implementation of capacitive proximity sensor using microelectromechanical systems technology *IEEE Trans. Indust. Electron.* **45** 886–94

[29] Hegg M C and Mamishev A V 2004 Influence of variable plate separation on fringing electric fields in parallel-plate capacitors *Int. Symp. on Electrical Insulation* pp 384–7

[30] Poinern G E J, Ali N and Fawcett D 2011 Progress in nano-engineered anodic aluminum oxide membrane development *Materials* **4** 487–526

[31] Masuda H, Yamada H, Satoh M, Asoh H, Nakao M and Tamamura T 1997 Highly ordered nanochannel-array architecture in anodic alumina *Appl. Phys. Lett.* **71** 2770–2